Akademie věd České republiky

Teze doktorské disertační práce
k získaní vědeckého titulu „doktor věd“
ve skupině věd – chemické vědy

Some Electrochemical Properties of Titanium(IV) Oxides and Carbon Nanostructures

Komise pro obhajoby doktorských disertací v oboru – fyzikální chemie

Jméno uchazeče: **Ladislav Kavan**

Pracoviště uchazeče: Ústav fyzikální chemie Jaroslava Heyrovského AV ČR

Místo a datum: Praha, červen 2005

Table of contents

Some Electrochemical Properties of Titanium(IV) Oxides and Carbon Nanostructures

Abstract

Novel preparative procedures towards Ti(IV) oxides were developed, and array of materials was synthesized ranging from quantum-sized nanocrystals up to macroscopic anatase single crystal. The obtained materials also comprise organized mesoporous layers, inverse opal, nanosheets and nanofibres from TiO_2, as well as nanocrystalline $Li_4Ti_5O_{12}$. Electrochemical properties of TiO_2 were investigated in the depletion regime both under the band-gap and sub band-gap photoexcitation. The latter approach generated data, relevant for the optimization of solar cells with dye-sensitized photoanode. Photoelectrochemistry and *in-situ* optical spectroelectrochemistry evidenced negative shift of flatband potential and blue shift of the band gap of Q-sized anatase, made by electrochemical synthesis. Dark electrochemistry in the accumulation regime was aimed at Li-insertion into TiO_2 and $Li_4Ti_5O_{12}$. The Li-storage depends significantly on the structure and morphology of Ti(IV) oxide host, and unique pseudocapacitive Li-storage was found in TiO_2(B) nanofibres. Novel Li-ion batteries were demonstrated implementing the concept of nanocrystalline host material.

Electrochemical synthesis of elemental carbon (electrochemical carbon) was explored *via* total dehalogenation of perhalogenated hydrocarbons by amalgams of alkali metals at room temperature. Depending on the precursor type, the electrochemical carbons can adopt the structure of carbyne-like materials, fullerenes and multiwalled carbon nanotubes. Electrochemical doping of carbonaceous nanostructures is superior to chemical redox doping by its versatility and precise control of the doping level. *In-situ* optical and Raman spectroelectrochemistry of single walled carbon nanotubes confirmed reversible and fast quenching of the electronic transitions between van Hove singularities, and evidenced the chirality- and counterion-dependent selectivity of this process. The Raman spectrum of intratubular C_{60} in a fullerene peapod was considerably enhanced by anodic doping, but not by cathodic doping. In contrast, the Raman spectrum of intratubular C_{70} in a peapod showed symmetric charge-transfer bleaching as the tube-related modes. A suggested interpretation follows from the electronic structure of the particular peapods. *In-situ* optical and Raman spectroelectrochemistry of double wall carbon nanotubes evidence that the outer tubes are more sensitive to electrochemical doping compared to inner tubes.

Part A: Titanium(IV) oxides

Principal works about electrode materials based on titanium(IV) oxides are presented in publications, which are enclosed to this thesis in Attachment . They are aimed at electrochemical preparation of anatase nanocrystals and at the investigation of their physical properties , highlighting the application in photoelectrochemical solar cells . Alternative preparative methods towards nanocrystalline anatase are spray pyrolysis , sol-gel and sintering of powder materials . More advanced materials are based on organized anatase nanocrystals; the ordering is achieved by stabilization with Zr , templating by polymeric surfactants or by latex-opal . Macroscopic anatase single crystal was prepared as a reference material for nanocrystalline anatase . A specific structural ordering of TiO_2 nanocrystals (anatase, rutile, TiO_2(B) and brookite) into nanosheets or nanofibres is achieved in syntheses employing protonic titanates as intermediates . A particularly interesting output of these syntheses is a phase-pure TiO_2(B) . Electrochemical , spectroelectrochemical and photoelectrochemical properties of the above mentioned materials were studied in detail. Besides the applications in solar cells , the Ti(IV) oxides can be used in Li-ion batteries. Hence, Li-insertion was studied systematically on nanocrystalline Ti(IV) oxides, both non-organized and organized materials, as well as on anatase single crystal electrodes . Promising Li-insertion performance was found for nanocrystalline oxide $Li_4Ti_5O_{12}$ (spinel) prepared by sol-gel route or from industrial powders . Below is an extended summary of these papers, along with some additional data collected on the subject.

1. ELECTRODE MATERIAS FROM Ti(IV) OXIDES: PREPARATION

Since the pioneering study in 1972 , titanium dioxide has been recognized as one of the most important materials for photoelectrochemistry . TiO_2 is attractive electrode material for practical applications, e.g. in photoelectrochemical solar cells, because of its low price, stability, and environmental compatibility. For solar energy conversion, TiO_2 needs to be sensitized by adsorption of suitable dyes . The first photoelectrochemical studies of TiO_2 in early 70s employed almost exclusively the n-doped rutile single crystal. This electrode material is not suitable for sensitization, because the monolayer of adsorbed dye on a flat surface does not absorb the light very efficiently . To increase the physical surface area per square unit of the projected electrode area (roughness factor), polycrystalline electrodes must be used . A logical conclusion is that small crystals (nanocrystals) are the optimum materials for TiO_2 electrodes in solar cells. Also for the application in Li-ion batteries, the nanocrystalline morphology is beneficial, especially if fast charging/discharging of a battery is requested. Obviously, there is a motivation for exploring of electrochemical properties of nanocrystals in general, and Ti(IV) oxides in particular.

1.1. Electrode materials from non-organized nanocrystalline Ti(IV) oxides

Despite the fact that rutile is considered to be the thermodynamically stable form of TiO_2 at normal conditions (by *ca.* 5-12 kJ/mol more stable than anatase) , this is true only for crystals larger than about tens of nm. (This is reminiscent of the known conclusion that the nanometer-sized diamond is more stable than graphite). Consequently, nanocrystalline rutile is a less-common material than nanocrystalline anatase. A model reaction producing nanocrystalline anatase is hydrolysis of titanium(IV) alkoxides:

$$Ti(OR)_4 + 2\ H_2O \rightarrow TiO_2 + 4\ ROH \qquad (1)$$

where R is alkyl; typically ethyl, butyl or isopropyl. This reaction makes a basis of sol-gel processes, yielding primary anatase nanocrystals. They are further processed by peptization (de-agglomeration), hydrothermal growth (Ostwald ripening) and sintering into layers (*ca.* 10 μm in thickness) of nanoparticles (10-20 nm in size) on certain substrate, e.g. F-doped SnO_2 or Ti . These films were suitable for solar cell applications and for Li-ion batteries . A somewhat simplified synthetic protocol was adopted in our earlier works on solar cells: the anatase layers were grown by repeated thermal decomposition of $Ti(OR)_4$ on top of Ti substrate .

The hydrolysis of alkoxides (Eq. 1) may also provide more complex materials, such as Zr-doped anatase (1-5 % Zr) . There have been numerous modifications of the model sol-gel process depicted by reaction (1). Hydrolysis of a mixture of Ti- and Li-alkoxides may lead to useful ternary oxide, $Li_4Ti_5O_{12}$ (spinel) :

$$5\ Ti(OR)_4 + 4\ LiOEt + 12\ H_2O \rightarrow Li_4Ti_5O_{12} + 20\ ROH + 4\ EtOH \qquad (2)$$

where R = isopropyl or butyl and Et = ethyl. The usual product of reaction (2) is a mixture of anatase with lithium titanates, but proper tuning of the synthetic conditions leads to a phase-pure spinel . The phase purity was confirmed by X-ray diffraction, Raman spectroscopy and electrochemistry . The sol-gel synthesis of $Li_4Ti_5O_{12}$ (spinel) provided the smallest so far obtained nanocrystals with surface areas of (183 - 196) m^2/g .

Electrochemically active layers of TiO_2 and $Li_4Ti_5O_{12}$ can be also fabricated by sintering of powder materials. This technique was first demonstrated on the material P25 (Degussa), which is a mixture of anatase and rutile . The key step in the preparation of electrodes consists in the disintegration of agglomerates with the aid of acetylacetone, which forms a complex with the TiO_2 surface . The same synthetic protocol was later employed for five other industrial TiO_2 powders having the BET surface areas between 14 to 404 m^2/g and the coherent domain sizes between 50 to 4 nm . Analogously, sixteen industrial powders of $Li_4Ti_5O_{12}$ (BET surface areas from 1.3 to 135 m^2/g; coherent domain sizes from 1300 to 19 nm) were used for fabrication of thin-layer electrodes according to the same deposition procedure . All these synthetic methods provide layers, which are not structurally organized. In other words, the morphology of layers can be characterized as that of statistically oriented particles of varying sizes, which are randomly interconnected into polycrystalline network.

1.1.1. Electrochemical deposition of anatase

Another preparative technique towards nanocrystalline anatase is based on anodic oxidative hydrolysis of aqueous solution of $TiCl_3$. At the pH between 2 to 2.5, the reaction starts from partly hydrolyzed species, $TiOH^{2+}$ (Eq. 3a). This is oxidized on a TiO_2 surface, and further hydrolyzed providing TiO_2 (anatase) as the final product (Eq. 3b).

$$Ti^{3+} + H_2O \rightarrow TiOH^{2+} + H^+ \qquad (3a)$$

$$TiOH^{2+} + H_2O - e^- \rightarrow TiO_2 + 3H^+ \qquad (3b)$$

Since TiO_2 grows on the previously deposited TiO_2 surface, the faradaic process can only occur *via* an electron injection from $TiOH^{2+}$ into the conduction band of TiO_2 . Anodic reactions on (non-illuminated) TiO_2 are, apparently, impossible above the flatband potential, i.e. they are restricted to redox couples with sufficiently negative redox potentials .

The described electrodeposition of TiO_2 offers various attractive features: (i) The layer growth is well controlled by the passed charge (although the faradaic efficiency is generally not 100 %, and is pH-dependent) ; (ii) The electrodeposited particles can be extremely small, exhibiting even Q-size effects ; (iii) The particles are formed from pure anatase, and can be efficiently sensitized for solar applications ; (iv) The electrodeposited films thinner than *ca.* 200 nm are defects-free, hence, the film is well adopted for blocking underlayers on F-doped SnO_2 substrate . This issue is critical for photoanodes in solar cells, where the parasitic reactions on the substrate must be minimized (cf. Section 3) . The reactions (3a, 3b) are also applicable for templated growth of anatase nanotubes , mosaic nano-arrays and inverse opal (Section 1.2.3) .

1.1.2. Aerosol pyrolysis

Another preparative procedure towards nanocrystalline anatase is based on the pyrolysis of an aerosol from ethanolic solution of di-*iso*-propoxy-titanium-bis(acetylacetone) . Similar to electrodeposition (cf. Section 1.1.1) this technique is also suitable for fabrication of blocking layers in solid-state TiO_2 solar cells . The crucial effect consists in preventing of the back electron transfer from the supporting material (e.g. F-doped SnO_2) into the hole-transport medium, which would short-circuit the cell (Section 3) . Recently, Peter et al. demonstrated that blocking of the back electron transfer *via* aerosol-pyrolyzed underlayers is equally significant also in liquid-junction solar cells, particularly at low light intensities. Another attractive feature of spray pyrolysis is its versatility; for instance the doping of TiO_2 by Fe or Nb can be carried out by only small modification of the synthetic protocol .

The prepared layers have generally the anatase structure; the size of coherent crystal domains is around 50 nm . They exhibit excellent photoelectrochemical performance of water oxidation . The high photoelectrochemical efficiency and easy fabrication of these TiO_2 layers makes them ideal for investigation of various other photoredox reactions beyond the water oxidation (cf. Section 4). Cameron and Peter presented a detailed treatment of electrochemical and photoelectrochemical properties of aerosol-pyrolyzed TiO_2 layers by impedance measurements, ellipsometry and voltammetry.

1.2. Electrode materials from organized nanocrystalline anatase

The sol-gel process, based on hydrolysis of Ti(IV) alkoxides (Eq. 1) hardly leads to organized structures (cf. Section 1.1). An exception to this rule has been accidentally found by Burnside et al. and further confirmed by Chemseddine and Moritz : Peptization of the TiO_2 colloid in $N(CH_3)_4OH$ caused selforganization of anatase nanocrystals. The selforganization was explained in terms of the Derjaguin-Landau-Verwey-Overbeek theory by balanced attractive/repulsive forces among particles . This interpretation, however, did not clearly address the absence of selforganization in other media, e.g. during the more common acidic peptization. Secondly, the selforganization of anatase was restricted only to a thin layer on top of the electrode surface (2-3 layers of particles) . To achieve better ordering of anatase, one has to choose different synthetic techniques, while the supramolecular templating is the most successful one.

1.2.1. Surfactant templating and stabilization with inorganic additives (Zr, Al)

The surfactant-templated synthesis of TiO_2 molecular sieves (an analogue of silica MCM41) was announced in 1995. This work was later questioned, because TiO_2 easily crystallizes during detemplating by calcination, while the organized texture collapses . A possible way out is stabilization of the TiO_2 structure by additional inorganic additive, such as zirconia . The particular material was grown from $(NH_4)_2Ti(OH)_2(C_3H_5O_3)_2$ and $(NH_4)_2Zr(OH)_2(CO_3)_2$, while cetyltrimethylammonium cation served as the structure-directing template . This synthetic protocol provides zirconia-stabilized TiO_2 (Zr/Ti = 1/3), called PNNL-1 (Pacific Northwest National Laboratory) . The material contained anatase crystallites, which were separated by a solid solution of amorphous $Zr_xTi_{1-x}O_4$. The morphology is characterized by mesoporous framework (surface area 330 m^2/g) with regular mesopores of the diameter of 3 nm. It exhibited enhanced thermal stability and interesting electrochemical properties as compared to those of ordinary (non-organized) nanocrystalline anatase .

The synthetic protocol of PNNL-1 was later extended to a preparation of alumina-stabilized TiO_2 mesoporous framework structure . The preparation started from $(NH_4)_2Ti(OH)_2(C_3H_5O_3)_2$, templated by cetyltrimethylammonium chloride, and Keggin cations, $Al_{13}O_4(OH)_{24}^{7+}$ served as precursor of the inorganic stabilizer. In contrast to PNNL-1 (which was pure anatase), the Al-stabilized materials exhibited unique core (anatase)/shell (rutile) structure. This unusual structure can be traced only by *micro*-Raman spectroscopy, but not by X-ray diffraction . The prepared materials exhibit increase of surface area with the Al-content (from 55 to 185 m^2/g). The mesopore volume increased in the same series, but the mesopore diameter was roughly uniform (from 2.4 to 2.6 nm).

There are various practical motivations for exploring of the TiO_2 materials stabilized by Al_2O_3 or ZrO_2. For instance, alumina coating is widely used for improving the photostability of TiO_2 (rutile)-based white pigments. Durrant et al. reported that Al_2O_3 or ZrO_2 coating on TiO_2 (anatase) prevents charge recombination in dye sensitized solar cells, which improves the efficiency of solar energy conversion. Aluminum is essential for stabilization of anatase single crystal (Section 1.3) . A special form of mesoporous alumina has been used as a template for the fabrication of anatase nanotubes and patterned arrays (cf. Section 1.1.1).

1.2.2. Templating with block copolymers

Further improvement of the template-aided synthesis of TiO_2 was pioneered by Stucky et al. . Thus prepared materials exhibited well organized mesoporous structure, without the inorganic stabilizer (cf. Section 1.2.1). The original synthesis was based on controlled solvolysis of $TiCl_4$ in EtOH (Et – ethyl):

$$TiCl_4 + x\ EtOH \rightarrow TiCl_{4-x}(OEt)_x + x\ HCl \qquad (4)$$

where $x \approx 2$. The templating surfactant was amphiphilic triblock copolymer of ethylene oxide and propylene oxide, such as Pluronic P123 (BASF):

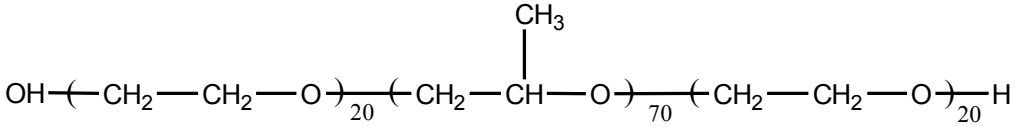

The $TiCl_{4-x}(OEt)_x$ units (Eq. 4) preferentially associate with the more hydrophilic block, i.e. ethylene oxide, which is the driving force for templating of a regular TiO_2. Ozin et al later improved the synthesis by using Ti(IV) ethoxide and buthanol instead of $TiCl_4$ and EtOH (Eq. 4). After calcination we have produced thin films (0.2-0.5 μm) of TiO_2 (208 m^2/g) on top of F-doped SnO_2 . They exhibited regular pores ~10 nm in size with continuous pore walls . This structure was reasonably robust, but did not survive long (~ 40 hours) heat treatment at *ca.* 450°C . The Pluronic-templated TiO_2 contains, reportedly, anatase nanocrystals (*ca.* 3 nm in size) embedded in "amorphous" framework structure . However, a careful inspection of Raman spectra points at an additional phase, which was only recently identified as monoclinic TiO_2(B) .

1.2.3. Templating by polystyrene spheres: anatase inverse opal

Polystyrene spheres with uniform diameter (d_p) form opal-like close packed structures (mostly *fcc*). They present a photonic crystal with the stop-band wavelength (λ_p):

$$\lambda_p = 1.633 d_p[(1-f)n_{air}^2 + fn_p^2]^{1/2} \qquad (5)$$

assuming light incidence normal to the (111) face of the *fcc* structure; n_{air} and n_p, are refractive indices of air and polystyrene, respectively and f is the fraction of volume filling, i.e. 0.74 for close packing of spheres. This treatment is applicable also for inverse opal from TiO_2. It is grown by filling of the voids between polystyrene spheres, which are finally removed by calcination . The inverse opal from TiO_2 anatase is attractive for optical photonic crystal applications due to its high refractive index. This also represents a challenge for dye-sensitized solar cell. If the stop-band position (Eq. 5) is adjusted to the optimum matching with solar spectrum and the optical absorption spectrum of the sensitizer dye, we could expect the increase of photocurrent efficiency by 26% .

TiO_2 was deposited inside the template by four methods : (i, ii) hydrolysis of titanium(IV) isopropoxide (cf. Eq. 1) which was deposited either from the (i) vapor phase or from (ii) propanolic solution, (iii) anodic oxidative hydrolysis of $TiCl_3$ (cf. Eqs. 3a, 3b) and (iv) liquid phase deposition from $(NH_4)_2TiF_6$ solution. The latter method employs hydrolysis in homogeneous medium, while the produced HF is scavenged by H_3BO_3:

$$TiF_6^{2-} + n\ H_2O \rightarrow [TiF_{6-n}(OH)_n]^{2-} + n\ HF \qquad (6a)$$

$$4HF + H_3BO_3 \rightarrow HBF_4 + 3H_2O \qquad (6b)$$

The methods (i), (ii), and (iv) allow the growth of inverse opal layers on non-conductive substrates or even self-standing. An interesting upgrade of method (i) consists in combined templating with block copolymers (cf. Section 1.2.2), and polystyrene opal, which leads to hierarchically organized TiO_2 structures). The electrodeposition (method iii) requires conductive support, e.g. F-doped SnO_2, but it benefits from precise control of the growth conditions and almost perfect filling of the template pores .

1.2.4 Organized TiO_2 nanostructures made from titanates

Kasuga et al. pioneered the synthesis of so-called "anatase nanotubes" *via* a hydrothermal conversion of TiO_2 into Na-titanate followed by Na^+/H^+ ion exchange and final calcination of the protonic titanate. This subject

provoked many follow-up studies, whose outputs were, however, often contradictory (for discussion see Refs.). We have explored this reaction in detail , while it turned out that anatase nanotubes (of comparable perfection to carbon nanotubes) were never demonstrated. Typical morphology is a fibrous nanosheet, either flat or curved . The parent materials are layered protonic titanates, $H_2Ti_xO_{2x+1}$ (x = 3, 4, 5), while $H_2Ti_3O_7$ is, presumably, dominating. The structure of $H_2Ti_xO_{2x+1}$ is characterized by corrugated ribbons containing 3, 4 or 5 TiO_6 octahedra in flat sections. Upon calcination, they convert to nanosheets containing anatase as the main phase, but rutile, brookite and TiO_2(B) are traceable, too .

An alternative route towards TiO_2 nanosheets starts from cesium titanate of the lepidocrocite structure, $Cs_xTi_{2-x/4}\square_{x/4}O_4$ (x ≈ 0.7; □ = vacancy), which is readily accessible from TiO_2 and Cs_2CO_3 . This material is ion-exchanged into $H_xTi_{2-x/4}\square_{x/4}O_4$ and finally calcined to TiO_2. It is characterized by ideally flat sheets of edge-sharing TiO_6 octahedra, while the nanosheet is formed from just two layers of TiO_6 octahedra . Despite the fact that $H_xTi_{2-x/4}\square_{x/4}O_4$ converts directly to anatase upon calcination, we have unexpectedly found that this synthesis may also provide phase-pure TiO_2(B) . The interpretation is obvious: besides the orthorhombic $Cs_xTi_{2-x/4}\square_{x/4}O_4$ (x ≈ 0.7) intermediate, we should also consider the monoclinic $Cs_2Ti_5O_{11}$. Apparently, the orthorhombic lepidocrocite or monoclinic pentatitanate are only distinguished by a small difference in the stoichiometry of reactants: Cs/Ti = 0.4 for pentatitanate, and Cs/Ti = 0.38 for lepidocrocite, respectively . By tuning of the synthetic conditions, the high-quality TiO_2(B) is readily accessible *via* this "pseudo-lepidocrocite route" . The produced material has a fibrous polycrystalline morphology, but the individual nanocrystals are organized, so that the *b*-axis of the TiO_2(B) lattice coincides with the fiber axis . This special structure is responsible for very peculiar electrochemical properties of TiO_2(B) nanofibre (Section 5.1).

1.3. Single crystal anatase electrode

Rutile single crystal was a material of the first choice for all early studies of TiO_2 electrodes, including the pioneering work by Fujishima and Honda in 1972 . The material is grown usually by Verneuiel method, and is commercially available in various orientations: (001), (100) or (110). On the other hand, there were only scarce data about anatase, which was caused by a lack of reasonably sized and pure anatase crystals. The crucial problem is, that the temperature during crystal growth must not exceed 700°C, when rutile is spontaneously formed. Consequently, macroscopic anatase crystals are grown by alternative low-temperature methods, such as chemical transport reaction in the TiO_2 (s) – $TeCl_4$ (g) system :

$$TiO_2 + TeCl_4 \rightleftharpoons TiCl_4 + TeO_2 \qquad (7)$$

The reversibility of reaction (7) allows using $TeCl_4$(g) as the chemical-transport medium for TiO_2: at certain temperature $T_1 > T_2$ the reaction proceeds faster from left to right, while at T_2 the back reaction is faster. The optimum values of T_1 and T_2 were 680°C and 640°C, respectively . The anatase crystal must be stabilized by certain additive, such as Al in concentration of (0.22-0.53) wt% . The crystal further contained "natural" impurities: 150-240 ppm Nb, 170-260 ppm V, 90-140 ppm Zr and 12-14 ppm La .

Anatase can be grown in the orientation of (101) and also (001) . For the fabrication of electrodes, the crystal must be n-doped by partial reduction in H_2 or H_2/Ar atmosphere . Alternatively, we can use also

electrochemical doping . AFM imaging confirmed that the corrugation of the crystal surfaces was typically below 1 nm. Only in accidental cases, steps or islands up to several hundreds nm were also observed at the (101) face . Anatase single crystal has been further characterized by XRD , ESCA, Raman spectroscopy, STM and STS as well as by variety of electrochemical and photoelectrochemical techniques . The major data from (photo)electrochemical characterization of anatase single crystal are compiled in Table 1.

Table 1: Electrochemical characteristics of anatase single crystal electrodes in the (101) and (001) orientations. MS = Mott-Schottky plot, CV = cyclic voltammetry, CHA = chronoamperometry.

Symbol	Quantity	units	(101)	(001)	**Ref.**
E_{fb}	Flatband potential @ pH=1 (MS)	V, *vs.* Ag/AgCl	-0.28	-0.34	
N	Density of donors (MS)	cm^{-3}	$2.5 \cdot 10^{19}$	$1.2 \cdot 10^{19}$	
C	Interfacial capacitance (CV)	$\mu F/cm^2$	(5 – 20)	-	
E_H	Onset of H^+ reduction (0.5 M HCl)	V, *vs.* Ag/AgCl	-0.22	-0.31	
D_{Li}	Diffusion coefficient for Li^+ (CV)	cm^2/s	$7 \cdot 10^{-14}$	$2 \cdot 10^{-13}$	
D_{Li}	Diffusion coefficient for Li^+ (CHA)	cm^2/s	$2 \cdot 10^{-13}$	$4 \cdot 10^{-13}$	
E_a	Activation energy for Li^+ insertion	eV	0.63	0.52	
k_0	Rate constant of Li^+ insertion (CV)	cm/s	$2 \cdot 10^{-9}$	10^{-8}	
E_{ph}	Onset of UV-photocurrent @ pH=1	V, *vs.* Ag/AgCl	-0.24	-0.28	
IPCE	**Photocurrent efficiency @ λ=300 nm**	**%**	**80**	**-**	

2. PHOTOELECTROCHEMISTRY: BAND-GAP EXCITATION

Titanium dioxide has an indirect band gap of 3.0 eV (rutile) , 3.2 eV (anatase) and (3 - 3.22) eV (TiO_2(B)) . This translates into the UV-light wavelengths of *ca.* 390-415 nm, which can create electron/hole (e^-/h^+) pairs in the material. Upon contact to electrolyte solution, a space-charge layer (thickness W) is formed underneath the TiO_2 surface. The electric field of space charge transports e^- to the bulk, and h^+ to the surface, where a photoanodic reaction, such as oxidation of water sets in. The incident photon to current conversion efficiency (*IPCE*) equals:

$$IPCE = \frac{i_{ph} h\nu}{Pe} \qquad (8)$$

where i_{ph} is the photocurrent density, h is Planck's constant, ν is the photon frequency, P is the incident light power density and e is the electron charge. Table 1 shows that *IPCE* as high as 80 % is accessible for anatase, while similar performance is traced also for rutile single crystal . The photocurrent density i_{ph} is assumed to be a limiting value at sufficiently positive potentials, when the band bending is large. If this is not the case, one has to consider also the potential (E) dependence:

$$i_{ph}^{\ 2} = \frac{2e\varepsilon_0\varepsilon_r P^2 \alpha_o^{\ 2}}{N}\left(E - E_{fb}\right) \qquad (9)$$

where α_o is the optical absorption coefficient, ε_0 is the permittivity of vacuum ε_r is the dielectric constant. This equation is useful for estimation of E_{fb} in addition to the impedance measurements (Mott-Schottky plot). Although we trace small deviation between impedance and photoelectrochemical data for anatase single crystal electrode (Table 1), they confirm that the E_{fb} is more negative for the (001) face compared to the (101) face . If we neglect the e^-/h^+ recombination in space-charge layer and assume the $W << 1/\alpha_o$ ($1/\alpha_o$ being the penetration depth of light) then:

$$IPCE = \frac{A_o e(L_h + W)(h\nu - E_g)^2}{h\nu} \qquad (10)$$

(A_o is an absorption constant, L_h is the h^+-diffusion length and E_g is the band gap). By comparing the E_g and flatband potential for rutile and anatase single crystal electrode (cf. Table 1) , it is obvious that the increased E_g of anatase affects only the position of valence band edge. In other words, the e^-/h^+ pairs can cause the splitting of water into H_2 and O_2 *only in anatase but not in rutile* . This conclusion is of fundamental significance, allowing rationalization of the classical problem of Fujishima and Honda .

Equation (10) is useful for determination of E_g in nanocrystalline materials. Although they normally behave like a single crystal electrodes, deviations appear for extremely small anatase crystals (1-2 nm), made by electrodeposition (see Section 1.1.1) or TiO_2 nanosheets . Such crystals exhibit increase (blue shift) of the band gap, ΔE_g, which matches the general equation for quantum confinement effect :

$$\Delta E_g = \frac{h^2}{8\mu_{xy}}\left(\frac{1}{L_x^2} + \frac{1}{L_y^2}\right) + \frac{h^2}{8\mu_z L_z^2} \qquad (11)$$

(μ is the reduced effective mass of the excitons and L corresponds to the crystal dimension. The subscripts x, y, and z denote directions of the crystal).

Polycrystalline anatase electrode, made, e.g. by thermal decomposition of Ti(IV) alkoxides show usually less good performance than the single crystals; the *IPCE* being *ca.* 30 % only . An outstanding exception to this rule is the TiO_2 (anatase) made by aerosol pyrolysis (cf. Section 1.1.2). This electrode material is so active for photoanodic water oxidation, that one could easily arrive at physically unrealistic conclusion that *IPCE* > 100% . To elucidate this paradox, one has to treat the absorption of UV-light in terms of the interfacial reflectivity, R_{ij} given by the Fresnel equation:

$$R_{ij} = \frac{(n_i - n_j)^2}{(n_i + n_j)^2} \qquad (12)$$

where n_i and n_j are complex refractive indices of the two materials forming an interface. Assuming the yield of charge injection (photoexcited h^+ to the electrolyte solution) to be 100 %, the *IPCE* can be approximated for TiO_2 films deposited on F-SnO_2 support as follows:

$$IPCE = 1\text{-}R_{12} + (R_{12}+R_{13}\text{-}R_{12}R_{13}\text{-}1)\cdot\exp(-\alpha\delta) - (R_{23}\text{-}R_{12}R_{23})\cdot\exp(-2\alpha\delta) \qquad (13)$$

δ is the TiO_2 film thickness and the indexes 1, 2, 3 denote TiO_2, electrolyte solution and F-SnO_2, respectively. Qualitatively, this equation depicts that the *IPCE* is decreased by reflection loss at the TiO_2/electrolyte solution interface but increased by reflection at the TiO_2/F-SnO_2 interface. Second, the Eq. (13) demonstrates that the light power penetrating the electrolyte/TiO_2 interface is by *ca.* 17 % larger compared to the air/TiO_2 interface, which is often (incorrectly) used as the reference for light harvesting efficiency . This provides rational for the explanation of the above mentioned paradox.

3. PHOTOELECTROCHEMISTRY: SUB-BAND-GAP EXCITATION

As shown in Section 2, titanium dioxide absorbs UV photons with $h\nu > E_g$, which, however, represents only *ca.* 4% of the solar power impinging to the Earth. Hence, for photoelectrochemical solar cells, TiO_2 needs to be sensitized to longer wavelengths, e.g. by $Ru(bpy)_3^{2+}$ (bpy = 2,2'-bipyridine) in the aqueous electrolyte solution . The crucial effect consists in the electron injection from photoexcited complex ($Ru^*(bpy)_3^{2+}$, formed at λ_{max} = 452 nm) into the conduction band of TiO_2. The by-produced $Ru(bpy)_3^{3+}$ is scavenged by hydroquinone, HQ to the starting $Ru(bpy)_3^{2+}$, while quinone, Q is formed:

$$Ru(bpy)_3^{2+} + h\nu \rightarrow Ru^*(bpy)_3^{2+} \rightarrow Ru(bpy)_3^{3+} + e^-_{CB}(TiO_2) \qquad (14a)$$

$$Ru(bpy)_3^{3+} + ½\ HQ \rightarrow Ru(bpy)_3^{2+} + ½\ Q + H^+ \qquad (14b)$$

The regenerative loop can be completed, if Q is reduced back to HQ by photogenerated electrons [$e^-_{CB}(TiO_2)$] at the Pt counter-electrode. The back electron transfer:

$$e^-_{CB}(TiO_2) + Ru(bpy)_3^{3+} \rightarrow Ru(bpy)_3^{2+} \qquad (14c)$$

is minimized by band bending. The sensitization by $Ru(bpy)_3^{2+}$ (Eqs. 14a-14b) is not very efficient (cf. Table 2). The reason is, that for the lifetime of the $Ru^*(bpy)_3^{2+}$ (t = 1.74 μs) and its diffusion coefficient, $D \approx 10^{-5}$ cm^2/s, the effective diffusion distance of $Ru^*(bpy)_3^{2+}$ is $(\pi t \cdot D)^{1/2} \approx 74$ nm . In other words, only the $Ru^*(bpy)_3^{2+}$ species in a close vicinity (< 74 nm) to the TiO_2 surface is active for reaction (14a); the rest just causes thermal dissipation of absorbed light in the solution. To minimize this parasitic effect, $Ru(bpy)_3^{2+}$ was confined in a thin film of perfluoro cation exchange polymer, Nafion (cf. Table 2) . (For further studies of Nafion and other pefluoro anion-exchange films, see, e.g. Ref.).

Table 2. Examples of liquid-junction solar cells employing sensitized TiO_2 as a photoanode. L = 2,2'-bipyridine-4,4'-dicarboxylate, EC = ethylene carbonate, PC = propylene carbonate, AN = acetonitrile.

TiO_2	Sensitizer	λ_{max} [nm]	Electrolyte	*IPCE* [%]	Φ_{sol} [%]	Ref.
Single crystal anatase	$Ru(SCN)_2L_2$	530	I^-/I_3^- + H_2O	0.11	<1[a]	
Thermal dec. $Ti(OR)_4$	$Ru(bpy)_3^{2+}$ (in solution)	452	HQ/Q + H_2O	2.6	<1[a]	
Thermal dec. $Ti(OR)_4$	$Ru(bpy)_3^{2+}$ (in Nafion)	452	HQ/Q + H_2O	8	<1[a]	
Thermal dec. $Ti(OR)_4$	RuL_3^{2+}	460	HQ/Q + H_2O	44	≈ 1[a]	
P25 + electrodep.	$RuL_2[\mu\text{-}(NC)Ru(CN)(bpy)_2]_2$	478	I^-/I_3^- + EC/PC	80	≈ 5[a]	
Sol-gel + electrodep.	$RuL_2[\mu\text{-}(NC)Ru(CN)(bpy)_2]_2$	478	I^-/I_3^- + EC/AN	85	7.12	
Sol-gel + electrodep.	$Ru(SCN)_2L_2$	530	I^-/I_3^- + AN	88	10.4	

[a] unpublished data

A considerable improvement was achieved, if $Ru(bpy)_3^{2+}$ was replaced by a complex $Ru(bpy)_2L^{2+}$; L = 2,2'-bipyridine-4,4'-dicarboxylic acid or RuL_3^{2+} which are strongly adsorbed on the TiO_2 surface. These works had provoked many follow up studies , but the state-of-art solar cells still employ this original philosophy . The best reported solar conversion efficiency of 10.4 % has been achieved with a similar sensitizer, $Ru(SCN)_2L_2$, and the HQ/Q redox relay was replaced by I^-/I_3^- in non-aqueous medium, such as acetonitrile (cf. Table 2) .

For optimum solar efficiency, the TiO_2 electrode must be sufficiently rough. The improvement in *IPCE* for rough TiO_2 surface can be demonstrated by a simple model calculation, assuming the extinction coefficient (ε) of $Ru(SCN)_2L_2$ dye (at λ_{max} = 530 nm) to be $1.27 \cdot 10^7$ cm^2/mol and the monolayer coverage of this dye, $\Gamma \approx 0.55$ molecules/nm^2. The *IPCE* of sensitized redox process is a product of quantum yield of charge injection, η_{inj} and the light-harvesting efficiency:

$$IPCE = \eta_{inj} (1\text{-}10^{-\Gamma\varepsilon}) \qquad (15)$$

which gives (at ideal conditions, for η_{inj} = 100%) the maximum theoretical *IPCE* to be 0.27% for a monolayer of $Ru(SCN)_2L_2$ on a flat surface. (Experimental value for a single crystal was 0.11 %, see Table 2). The nanocrystalline electrode can be modeled as a layer (thickness δ) of close-packed spheres (diameter *d*) deposited on conducting support, such as F-SnO_2. Then:

$$IPCE = \eta_{inj}\left(1 - 10^{1.48\delta\varepsilon\Gamma/d}\right) \qquad (16)$$

If we fix δ = 10 μm and η_{inj} = 100%, we obtain *IPCE* = 69 % (for *d* = 100 nm) and *IPCE* = 99 % (for *d* = 10 nm). The modeled values (δ = 10 μm *d* = 10 nm) are close to the experimentally optimized ones . Further improvement of the surface roughness was achieved by electrodeposition (cf. Section 1.1.1) of ultrasmall anatase crystals (1-2 nm in size) on top of the "ordinary" anatase nanocrystals made by sol-gel (10-20 nm) or from P25 . In practical cells, the blocking underlayers, made either by electrodeposition or spray pyrolysis enhance the cell performance by impeding the back electron transfer (Eq. 14c). This issue is particularly important for solid-state solar cells .

Although *IPCE* is useful parameter in evaluation of solar cells, a more practical criterion is the total solar conversion efficiency, ϕ_{sol} defined as the maximum electric power output (current × voltage) divided by the white light solar power (for AM1.5, the conventionally used value is 1000 W/m^2). There are various other practical issues to be addressed in real solar cells, such the cell geometry , light intensity and heat loses, including the effect of wind . Table 2 compiles several examples of solar cells. They all comprise the classical liquid-junction solar cells. A new design of solar cells is based on replacing the liquid electrolyte by solid hole-conducting medium, such as CuSCN or spiro-bis-fluorene derivatives . Their efficiency is not yet competitive (*IPCE* = 33%, ϕ_{sol} = 2.56 %) , but they are advantageous by higher stability and easy fabrication, e.g. on plastic substrates.

4. SPECTROELECTROCHEMISTRY

Thin layers of TiO_2 deposited on F-doped SnO_2 are optically transparent, which makes them useful for *in-situ* optical (UV-Vis) transmission spectroelectrochemistry. Particularly valuable is the measurement at potentials near the E_{fb}, when a broad band of conduction-band electrons appears at 600-650 nm . This further causes bleaching of interband transitions near the absorption threshold (Burnstein shift) . Both effects are applicable for

determination of E_{fb} in nanocrystalline materials, where the standard impedance techniques often fail because of frequency dispersion and non-linear Mott-Schottky plot . Nevertheless, certain materials, such as TiO_2 made by aerosol pyrolysis (Section 1.1.2), do allow some comparison of both techniques . The spectroelectrochemical method evidenced negative shift of E_{fb} in quantum-sized anatase crystals made by electrodeposition (the shift of E_{fb} was *ca.* 0.2 V compared to "normal" size anatase) . An almost identical E_{fb} shift was confirmed in TiO_2 nanosheets, where the Q-size effect influences only one coordinate (cf. Eq. 11) .

In-situ Raman spectroelectrochemistry on single crystal anatase turned to be useful technique for evaluation of the course of electrochemical doping . *In-situ* infrared spectroelectrochemistry at nanocrystalline TiO_2 was applied for monitoring of cathodic breakdown process in the solution $LiCF_3SO_3$ + propylene carbonate , which is of practical interest for Li-ion batteries. *In-situ* FTIR spectroelectrochemistry evidences that the solvent decomposes below 1.2 V *vs.* Li/Li^+ in the presence of trace water:

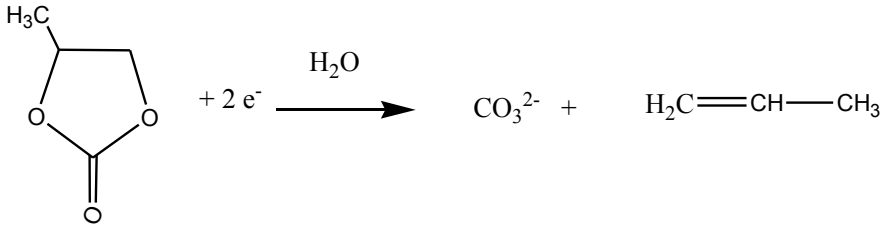

(17)

In-situ FTIR spectroelectrochemistry was also used for investigation of the photoanodic breakdown processes at the TiO_2 electrode illuminated by UV-light . The photoanodic oxidation of propylene carbonate , acetonitrile , dimethylsulfoxide and 3-methyl-oxazolidin-2-one was studied in detail on spray-pyrolyzed TiO_2 (Section 1.1.2). In all cases, CO_2 is traced as the final product, but additional intermediates can be also monitored, allowing discussion of the breakdown mechanism of these common solvents for aprotic electrolyte solutions . As expected, the photoanodic reactions give different products than the cathodic ones. For instance, propylene carbonate decomposes photoanodically to CO_2, acetone and unidentified polymers, but not to CO_3^{2-} nor to propylene (cf. Eq. 17) .

5. ELECTROCHEMISTRY IN THE ACCUMULATION REGIME

The depletion regime of TiO_2 is most often studied by photoanodic reactions (Sections 2 and 3). On the other hand, the accumulation of electrons in the space-charge layer can be studied electrochemically also in the dark. Four examples of faradaic processes on TiO_2 electrodes in the accumulation regime were already discussed above: (i) the reduction of $Ti(OH)^{2+}$ leading to electrodeposition of TiO_2 (Section 1.1.1) , (ii) water reduction applicable to the estimation of E_{fb} , (iii) electrochemical n-doping (Section 1.3) and (iv) cathodic decomposition of propylene carbonate (Section 4) .

5.1. Capacitive processes

The obvious process in the accumulation regime is double-layer charging at potentials below E_{fb}. It can be most simply monitored by cyclic voltammetry . The voltammetric current (I) of double layer charging scales with the first power of scan rate (v):

$$I = \frac{dQ}{dt} = C\frac{dE}{dt} = Cv \qquad (18)$$

where Q is the voltammetric charge and C is capacitance. The capacitance is typically 4- 15 μF/cm^2 in aprotic solutions containing Na^+, K^+, Cs^+ and NBu_4^+ (Bu = butyl), but increases by order of magnitude in aqueous medium, due to the H^+/OH^- exchange reactions in surface hydroxyls .

In the presence of Li^+ the mechanism of charge accumulation is different from just the capacitive process (Eq. 18), since both anatase and rutile accommodate Li^+ also in the bulk crystal (cf. Section 5.2). From this point of view, the nanofibres from monoclinic TiO_2(B) exhibit very unusual behavior . The Li-storage in TiO_2(B) obeys formally Eq. 18, but the charge exceeds that of double-layer capacity. It is, actually, comparable, or even higher, than the charge corresponding to the bulk Li^+ insertion in the TiO_2 (anatase, rutile) lattice. An attractive issue is that the charging of TiO_2(B) is not kinetically controlled by solid-state diffusion (Section 5.2) . This peculiar pseudocapacitive Li-storage was discussed in terms of the channel-structure of TiO_2(B) fiber. Two effects were considered: (i) fast Li^+ transport in the open channels running parallel to the b-axis (fiber axis) and (ii) reversible trapping of Li^+ ions at two different sites in the lattice . Both effects must occur simultaneously; this is indirectly evidenced by the fact that two other channel titania structures, i.e. TiO_2 (ramsdellite) and TiO_2 (hollandite) do not seem to show this pseudocapacitive Li-storage .

5.2 Li-insertion electrochemistry

The interest in Li-insertion electrochemistry has been motivated by practical applications in Li-batteries. We have demonstrated a 2-V rocking-chair (Li-ion) battery with nanocrystalline TiO_2 (anatase) anode accumulating lithium:

$$TiO_2 + x\,(Li^+ + e^-) \rightarrow Li_xTiO_2 \quad ; x \approx 0.5 \qquad (19a)$$

The cathodes were from common “4V” materials, i.e. $LiMO_2$ (M is Ni, Co or $Co_{0.5}Ni_{0.5}$) . Hence, the overall cell reaction for charging/discharging was:

$$TiO_2 + LiMO_2 \rightleftharpoons Li_xTiO_2 + Li_{1-x}MO_2 \qquad (19b)$$

The optimized battery delivered up to 55 mAh/g. This compares well to the charge density of similar battery with carbon anode, but the achieved energy density (106 mWh/g) is roughly half of that of the C/$LiMO_2$ battery, because of smaller voltage of the $TiO_2/LiMO_2$ system . However, TiO_2 anode is favored by higher safety, as the Li_xTiO_2 does not cause ignition like Li_xC, and the battery is also more stable against overcharging .

Accommodation of lithium in anatase is controlled by Li^+ diffusion between two-intermixed host phases (*I*41/*amd* and *Imma*) . The advantage of nanocrystalline host for Li-insertion batteries is documented by simple estimation of the diffusion layer thickness (d_D) for Li^+ underneath the TiO_2 surface.

$$d_D = \sqrt{\pi D_{Li} t} \qquad (20)$$

Assuming the solid state diffusion coefficient of Li^+ in anatase, $D_{Li} \approx 10^{-13}$ cm^2/s (see Table 1), then the charging time t equals about 300 s for d_D = 100 nm, but $t \approx 3$ s for d_D = 10 nm. In other words, an anatase crystal of

dimensions ($2\times d_D$) = 20 nm is fully loaded with Li^+ in several seconds, but a ten times larger crystal requires 100 times longer time for full charging with Li^+. Although this model calculation neglects the dependence of D_{Li} on the particle size (*vide infra*) , the benefits of nanocrystalline Li-insertion host are clearly demonstrated. (In this context, we may recall the discussion in Section 3 (Eq. 16), where we came to phenomenologically identical conclusion about the improvement of efficiency of solar cells with decreasing size of the TiO_2 particle. Albeit the physical backgrounds for both conclusions are different (Eqs. 16, 20), the gain in performance of *both* devices, i.e. solar cells and Li-ion batteries employing nanocrystalline TiO_2, is obvious.)

Even more promising anode material for Li^+-storage is based on the $Li_4Ti_5O_{12}$ (spinel), which reacts analogously to TiO_2 (cf. Eq. 19a) :

$$Li_4Ti_5O_{12} + 3\ e^- + 3\ Li^+ \rightleftharpoons Li_7Ti_5O_{12} \qquad (21)$$

The charging of $Li_4Ti_5O_{12}$ (Eq. 21) is faster than the charging of TiO_2 (Eq. 19a). A thin-layer electrode (2-4 μm) delivered up to 80 % of its nominal capacity (Eq. 21) even at the extreme charging rate of 250C . The benefit of nanocrystalline material is demonstrated by the linear dependence of charge capability (at 50C - 250C) with the logarithm of surface area for particles having surface areas < 20 m^2/g), while a plateau in optimum performance was observed for smaller particles surface (from 20 to 100 m^2/g) .

The insertion of Li into Ti(IV) oxides is attractive also for addressing more fundamental academic questions. The kinetics of reactions (19a, 21) is controlled by solid-state diffusion of Li^+. In cyclic voltammetry, the insertion/extraction peak current (I_p) scales with square root of the scan rate, v :

$$|I_p| = 0.4958nFAc\,(D_{Li}\alpha nFv/RT)^{1/2} \qquad (22)$$

(n is number of electrons, A is the electrode area, c is the maximum concentration of Li^+ in the accumulation layer (0.024 mol/cm^3 for x = 0.5; cf. Eq. 19a), α is the charge-transfer coefficient, and the other symbols have their usual meaning). In potential-step chronoamperometry, the insertion/extraction current (I) obeys the Cottrell equation :

$$|I| = AFD_{Li}^{1/2}c\pi^{1/2}t^{-1/2} \qquad (23)$$

The equations (22, 23) provide two independent techniques for determination of D_{Li}. (Still another technique is galvanostatic intermittent titration). The best defined results were obtained for anatase single crystal . We could even trace an anisotropy in Li-transport normal to the (101) and (001) anatase faces (Table 1) . It can be interpreted in terms of the Li^+ hopping between pseudo-octahedral position in the anatase lattice .

For assessment of the quality of Li-insertion host, we can also determine the standard rate constant of charge-transfer, k_0. The voltammetric peak current I_p scales with the peak potential, E_p :

$$|I_p| = 0.227AnFck_0 \exp\left[\frac{-\alpha nF(E_p - E_f)}{RT}\right] \qquad (24)$$

where E_f is the formal potential of insertion/extraction. Also in this case, we observe the same trend in Li-insertion rate at the (101) and (001) faces of anatase (Table 1) .

The matching of voltammetric and chronoamperometric values of D_{Li} is less good for nanocrystalline anatase , while D_{Li} decreases by orders of magnitude. Analogously, the rate constants, k_0 (Eq. 24) decrease for anatase nanocrystals by orders of magnitude compared to the values of single crystal (Table 1) . Slower Li-insertion was

also found for nanocrystalline $Li_4Ti_5O_{12}$ (spinel) with a monotonous drop of D_{Li} for decreasing particle size . However, the sluggish Li-storage in nanocrystals need not be detrimental for the overall charging rate of the electrode . The reason is that slower Li-diffusion and smaller rate constants for nanocrystals (both TiO_2 and $Li_4Ti_5O_{12}$), are more than compensated by the increase of the active electrode area . In other words, the bulk of solid is less important in small nanocrystals. They virtually extrapolate to a 2-D system, exhibiting surface-confined (pseudocapacitive) Li storage only . (For further discussion of pseudocapacitive Li-storage see Section 5.1 and Ref.).

5.2.1. Organized structures: S-peaks

The effects associated with Li-insertion are particularly useful for investigation of organized TiO_2 materials . The Li-insertion electrochemistry of anatase inverse opal evidenced that the charge propagation is hindered due to limited inter-particle necking . This conclusion raises some doubts about the predicted application of inverse opal in high-drain devices like solar cells , where currents of the order of 10 mA/cm^2 must be expected for a 10% solar cell at the full Sun illumination (cf. Section 3).

The surfactant templated mesoporous anatase, stabilized by Zr , Al and non-stabilized one exhibit specific voltammetric features at potentials between *ca.* 1.3 to 1.6 V . They are missing in ordinary anatase, and we have suggested calling these features "S-peaks" (with "A-peaks" standing for ordinary anatase) . The name comes from the fact that they behave like surface-confined charge-transfer. This is documented by (i) very small (E_p-E_f) splitting (even smaller that 30 mV expected for reversible diffusion-controlled process, Eqs. 22, 24) and by the capacitive-like $I(v)$ dependence (Eq. 18).

The S-peaks also occur in crystalline-glass nanocomposite TiO_2-P_2O_5 , nanorods nanotubes and inverse opal . They were originally discussed as a consequence of the presence of amorphous titania in the highly-organized mesoporous skeleton . Nevertheless, our further studies of titania nanosheets and nanofibres provided arguments for different interpretation. The pseudocapacitive Li-storage can be reasonably assumed in nanosheets, exhibiting even 2-D quantum confinement effects (cf. Eq. (11)) and nanofibrous TiO_2(B), which virtually behaves like a nanosheet, too (cf. Section) . We could even propose that the S-peaks evidence the presence of TiO_2(B) in all so far S-active materials , albeit this logical link was not considered prior to our detailed work on TiO_2(B) . The obvious reason is that TiO_2(B) may easily be unnoticed in a mixture with large concentration of anatase, because of an overlap of the main diagnostic XRD peaks, especially in nanocrystalline materials with broad diffraction maxima . This conclusion, on the other hand, demonstrates excellent analytical sensitivity of Li-insertion electrochemistry for mixture of nanocrystalline TiO_2 phases. Other examples of the unique electrochemical "phase analysis" is the detection of trace rutile in anatase and trace anatase in $Li_4Ti_5O_{12}$.

References to Part A. (References 1-13 are attached to the thesis *in extenso*)

Part B: Carbon

Principal works on carbon materials are described in publications, which are enclosed to this thesis in Attachment . They are focused on electrochemical preparation of carbons (electrochemical carbons) and on the investigation of their physical, structural and spectroscopic properties . The significance of electrochemical carbonization is highlighted by successful preparative demonstration of carbyne-like materials , fullerenes , carbon nanotubes and well-defined carbon films *via* this synthetic strategy. Selected pure nanocarbons, *viz*. single walled carbon nanotubes (SWCNT) , double walled carbon nanotubes (DWCNT) and fullerene peapods have been further studied systematically by using *in-situ* optical and Raman spectroelectrochemistry. Below is an extended summary of these papers, along with some additional data collected on the subject.

1. ELECTROCHEMICAL CARBON: PREPARATION

Electrochemical carbon (the term introduced in Ref.) denotes "synthetic solids consisting mainly of atoms of elemental carbon, which can be prepared electrochemically from suitable precursors". The preparation of electrochemical carbon does not require high temperatures and/or pressures, as the traditional (pyrolytic) syntheses of elemental carbon, since electrochemical carbonization of suitable precursors is thermodynamically favored even at ambient conditions ("soft chemistry") . It requires either unstable reactants (e.g. alkali metals) or reactive precursors (e.g. oligoynes) . Electrochemical carbonization is characterized by three specific features: (i) Production of unstable carbon chains, which are not likely to survive at high temperatures . (ii) Easy templating of carbon nanostructures by the precursors, allowing tailored syntheses of carbyne-like chains , fullerenes and nanotubes . (iii) Defined kinetics of certain reactions, yielding carbon films with precisely controlled thickness .

1.1 Electrochemical ways to carbyne-like chains

Carbyne denotes an ill-defined carbon crystal, whose structure is derived solely from *sp*-bonded all-carbon chains . Jansta and Dousek have suggested that electrochemical reductive carbonization of poly(tetrafluoroethylene) (PTFE) could be a pathway to such structures, and they have pioneered this reaction from the viewpoint of its mechanism and kinetics . The process inherently includes natural stabilization of polyyne by interspersed alkali metal fluoride, MF :

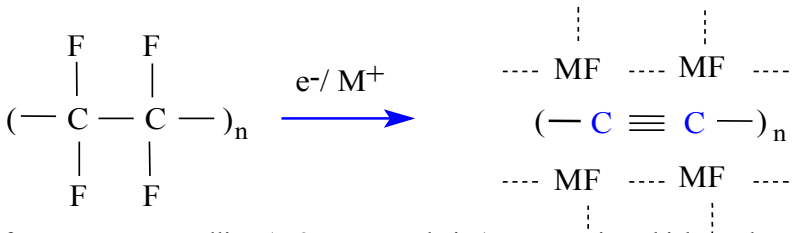

(1)

The latter forms a nanocrystalline (≈ 3 nm crystal size) MF matrix, which partly protects the carbynoid skeleton against cross-linking and/or external chemical attack . Reactivity towards O_2 , Br_2 , NH_3 , NO , S and carbenes has been studied in detail. A pure carbon from C-MF was also found to be a very efficient adsorbent .

The Jansta and Dousek's reaction occurs at the interface of PTFE and liquid amalgam of alkali metal, $M_{(Hg)}$ (M = Li, Na, K). A more detailed inspection of the reaction (Eq. 1) shows that there is a small superstoichiometric over-reduction, which can be considered as n-doping . Hence, the final product of reaction (Eq. 1) is a carbon containing some negative charge, $C^{\delta-}$ compensated by M^+ (the doping level, δ is between 0.05-0.45, most usually around 0.2):

$$C + \delta\, e^- \rightarrow C^{\delta-} \qquad (2)$$

PTFE does not react with Mg-amalgam according to the electrochemical mechanism (*vide infra*). Instead, we observe only thin-layer chemical carbonization without any electrochemical propagation . Also the Jansta and Dousek's electrochemical mechanism is perturbed, if the reaction is carried out with suspension of alkali metals instead of amalgams. In the case of alkali metal amalgams, the reaction is initiated by a fast chemical reduction, which produces the first monolayers of carbon-alkali metal fluoride (further denoted as C-MF). The C-MF layer is compact, non-porous and impermeable to the amalgam. However, it exhibits both electronic and ionic (M^+) conductivities, i.e. a short-circuited galvanic cell is formed spontaneously at the interface: $M_{(Hg)}$ | C-MF | PTFE. The C-MF layer acts simultaneously as a solid electrolyte , electron conductor and electrode . During the self-discharge, the carbonization of PTFE takes place at the carbon (C-MF) cathode, which is continuously renewed *in-situ* as the C-MF layer grows. The cathodic process consists of C-F bonds splitting (Eq. 1), while the fluoride anions formed subsequently recombine with M^+ cations, that also passed through the C-MF layer. If we neglect the n-doping (Eq. (2)) the cell voltage, ΔE equals:

$$\Delta E = \frac{\Delta G_{PTFE} - \Delta G_{MF} + 2F(E_{am} - E_0) + 2RT\ln c}{2F} \qquad (3)$$

where ΔG_{PTFE} and ΔG_{MF} are the Gibbs energies of PTFE and MF, E_0 is standard redox potential of alkali metal, E_{am} standard redox potential of the amalgam, and c amalgam concentration. Analysis shows that the reaction (1) is thermodynamically favored for PTFE and for some other precursors/reactions already at room temperature . The current (I) flowing through the cell can be expressed according to Faraday's law, but it is also controlled by the serial combination of ionic (σ_i) and electronic (σ_e) conductivities of C-MF:

$$I = \frac{ySL\rho F}{tMa} = \frac{S\Delta E\sigma_e\sigma_i}{L(\sigma_e + \sigma_i)} \qquad (4)$$

y is the number of electrons, S is the area of the (PTFE | amalgam) interface, L is the thickness of carbonized layer, ρ is the density of PTFE, t is the time, M is the molar mass of PTFE unit and a is a dimensionless structural factor. This expression gives:

$$L = \sqrt{\frac{\Delta EaM\sigma_e\sigma_i t}{yF\rho(\sigma_e + \sigma_i)}} = K_0 \cdot t^{1/2} \qquad (5)$$

where K_0 is a rate constant (Table 1).

Table 1. Reaction of alkali metal amalgams with fluoropolymers. Values of rate constant, K_0 (Eq. (5)).

PRECURSOR	Amalgam	K_0 [nm/s$^{1/2}$]	Reference

		25 ºC	100 ºC	
PTFE	Li	47.5	351	
PTFE	Na	2.67	16.7	
PTFE	K	0.1	3.7	
PTFE	Mg	<0.01	<0.01	
PCTFE	Li	124	1640	
NAFION 117	Li	15.3	115	
PTFE-PPVE	Li	38.3	360	
FEP	Li	47.0	-	
FEP	Na	2.7	-	
FEP	K	0.1	-	
PPO	Li	40	-	

PCTFE = poly(chlorotrifluoroethylene)
PTFE-PPVE = poly(tetrafluoroethylene-co-perfluoropropylvinylether)
FEP = poly(tetrafluoroethylene-co-hexafluoropropene)
PPO = perfluoropropenoxide

1.1.1 Evidence for the formation of electrochemical polyyne

The presence of polyyne in electrochemical carbon has been first convincingly demonstrated by Raman spectroscopy . The diagnostic band of C≡C stretch at ≈ 2000 cm^{-1} is, obviously, missing in the spectra of common carbon allotropes. By screening of various perfluoro-n-alkanes (C_xF_{2x+2}, x = 1, 2, 6, 9, 20, 24, ≈ ∞) the best yield of carbyne was found for PTFE and Na or K-amalgams . Even though the carbonization is always stoichiometrically quantitative (cf. Eq. 1), the polyyne can hardly be obtained in pure form . The actual products of reaction (1) are mesoscopic sp^2 carbons with short oligoyne sequences ($n < \approx 8$) . Polyyne is spontaneously cross-linked to graphene:

(6)

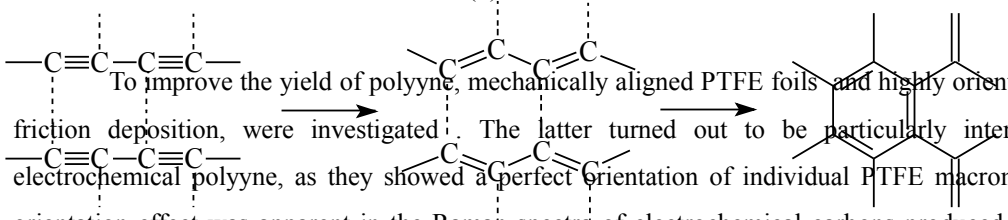

To improve the yield of polyyne, mechanically aligned PTFE foils and highly oriented films, prepared by friction deposition, were investigated . The latter turned out to be particularly interesting precursors of electrochemical polyyne, as they showed a perfect orientation of individual PTFE macromolecules , and some orientation effect was apparent in the Raman spectra of electrochemical carbons produced from stretch-oriented foils . The Raman spectra demonstrate better yield of polyyne from oriented precursors, the best conjugation length was estimated to be *nine triple bonds* . The yield of polyyne cannot be determined absolutely from Raman spectroscopy, because of resonance enhancement. To address this problem, selective reactions of polyyne with *in-situ* generated carbenes were employed . The yield of polyyne varied between 5-40 % for various samples and analytical methods; chemical analysis *via* carbenes evidences the yields to be better than 7 % .

A more detailed Raman study indicated a downshift of the intensity of the C≡C line and blue-shift of its frequency (i.e. decrease of the conjugation length), if a freshly prepared C-MF sample was stored in vacuum at room temperature . The aging rate decreased in the series: Li > Na > K. It can be further monitored by long-time (years) decreases of electronic resistivity ,

photoluminescence intensity and UV-Vis absorption . These changes are controlled by well-defined kinetics, and accelerate upon heating and especially after extraction of MF from the C-MF composite . All these features lead to a self-consistent structural picture: Polyyne, formed by reaction (1), decomposes to graphene (reaction 6); the cross-linking rate being controlled by a spatial separation of polyyne chains with interspersed MF.

1.2 Conversion of carbyne-like chains into nanotubes

The cross-linking of *sp*-chains into graphene (Eq. 6) is, apparently, undesired for the synthesis of carbyne, but it may be useful for synthesis of other nanocarbons. The production of nanotubes by cross-linking of the *ex*-PTFE electrochemical polyyne (Eqs. 1, 6) was first reported by Yasuda *et al.* . A similar strategy follows from pure low-molecular oligoynes, such as 1,3,5-hexatriyne and its derivatives , which may replace the poorly defined *ex*-PTFE polyyne (Eqs. 1, 6). Indeed, the nanotubes were obtained by spontaneous polymerization/carbonization of 1,3,5-hexatriyne and 1-iodo-1,3,5-hexatriyne . Similar nanotubes were demonstrated also *via* polymerization of dialkali hexatriynides . Higher or lower homologues of hexatriyne did not provide nanotubes , although they also polymerize spontaneously to give various forms of carbons .

1.3. Direct electrochemical synthesis of fullerenes and nanotubes

Total electrochemical dehalogenation of perhalogenated hydrocarbons may serve not only for production of carbyne-like chains (from perfluoro-n-alkanes), but it may present a pattern for synthesis of other interesting nanocarbons. Small amounts of fullerene C_{60}, C_{70}, onions and nanotubes were prepared *via* total dehalogenation of gaseous perfluoronaphthalene ($C_{10}F_8$), perfluorodecalin ($C_{10}F_{18}$) and perfluorocyclopentene (C_5F_8) with liquid amalgams of alkali metals at room temperature . A model conversion of perfluoronaphthalene into fullerene C_{60} is described by an overall reaction scheme:

6 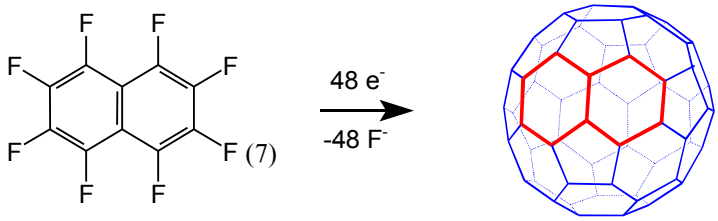

(7)

An analogous reaction was also found for perfluorodecalin . C_{60} can also condense from twelve C_5 radicals derived from perfluorocyclopentene:

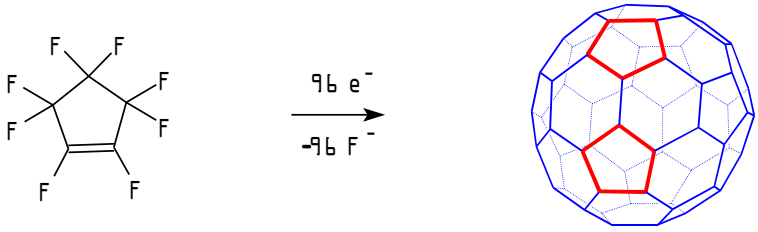

 (8)

Perfluorocyclopentene, perfluorodecalin and perfluoronaphthalene carbonized by Li-amalgam gave fullerene C_{60} in yields of *ca.* 0.1%, referred to the total amount of carbon produced (Eqs. 7, 8). The best yield of C_{60} was 0.36% in one batch from C_5F_8/Li-amalgam . Fullerene C_{60} and small amounts of C_{70} were detected in toluene extracts by HPLC, UV-Vis spectra and by mass spectroscopy . Similar to Eqs. 7, 8, total dehalogenation of hexachlorocyclopentadiene and hexachlorobenzene by potassium provides fullerene onions and nanotubes . Also diamond can be grown by dehalogenation of CCl_4 with Na .

Transmission electron microscopy also revealed the occurrence of graphite onions of diameters 20-100 nm in defluorinated C_5F_8 . The micrographs further showed capped multiwalled tubes, typically 15 nm in diameter and about 50-200 nm long. Whereas the tubes from C_5F_8 were straight, the tubes from $C_{10}F_{18}$ and $C_{10}F_8$ were curly and substantially longer. The concentration of nanotubes was about 1-2 % of the total amount of carbon produced. The occurrence of carbon onions was also mentioned in carbons made from hexatriyne precursors . The yield of electrochemical synthesis of fullerenes and nanotubes is not yet competitive to that of traditional synthetic procedures based on catalytic processes in carbon arc, laser ablation, CVD, HiPco etc. However, these reactions give the first evidence that *fullerenes, onions and nanotubes can be prepared by a non-catalytic "soft chemical" process at room temperature* . Later studies have demonstrated electrochemical synthesis of carbon nanotubes and onions from acetylene in liquid ammonia at -40 ºC , which is, presumably the lowest record. Nanotubes and nested fullerenes were also prepared by a non-catalytic reaction from supercritical CO_2 and Mg .

1.4. Kinetics and mechanism of electrochemical carbonization: refined model

The reactions described by Eqs. (7, 8) are governed by interesting kinetics. Generally, a spontaneous film-forming carbonization process towards C-MF occurs, if the surface of liquid amalgam of Li or Na is exposed to a vapor of perfluorinated hydrocarbon . The reaction is stoichiometric (super-stoichiometric) as in the case of PTFE (cf. Eqs. (1,2)). The film exhibits uniform interference color, hence, the film thickness, δ can be simply monitored *in-situ* by the interference fringes in UV-Vis reflectance (for $\delta\upsilon < \approx 2$ μm, υ is the refractive index) . Except for perfluoro-2-butyne (*vide infra*), the carbonaceous film grows linearly with time on the $Li_{(Hg)}$ surface:

$$\delta\upsilon = K_{Li}\, t \qquad (9)$$

but followed the "normal" kinetic behavior for Na-amalgam:

$$\delta\upsilon = K_{Na}\, t^{1/2} \qquad (10)$$

K_{Li} and K_{Na} are rate constants (Table 2). To interpret the kinetic discrepancies, (Eqs. 9, 10), an upgraded model was developed . The interfacial reaction is still governed by an electrochemical mechanism (Eqs. 3-5), but the cell voltage (E) is a sum of the activation voltage (E_a) and the ohmic drop at C-MF (E_Ω):

$$E = E_a + E_\Omega \qquad (11)$$

Note that the classical Jansta and Dousek's model of the fluoropolymer | $M_{(Hg)}$ interface (Eqs. (3-5)) considered only E_Ω but neglected E_a . As the current (I) is controlled by the activation voltage and conductivity, the Eq. 4 is more rigorously formulated:

$$I = \frac{ySL\rho F}{tMa} = I_0 \exp\left(\frac{\alpha yF}{RT} E_a\right) = \frac{SE_\Omega \sigma_e \sigma_i}{L(\sigma_e + \sigma_i)} \tag{12}$$

(α is the charge transfer coefficient and I_0 the exchange current). This gives:

$$E = \frac{RT}{\alpha yF} \cdot \ln \frac{SL\rho yF}{I_0 tMA} + \frac{L^2 \rho yF(\sigma_e + \sigma_i)}{\sigma_e \sigma_i Ma} \tag{13}$$

which cannot be solved analytically. For large E_a (or $L \rightarrow 0$), the second term is negligible:

$$L \approx \frac{I_0 tMa}{S\rho yF} \cdot \exp\left(\frac{\alpha yFE}{RT}\right) = K_1 \cdot t \tag{14}$$

Analogously, for $E_a \rightarrow 0$ (or $L >> 0$) the first term is negligible:

$$L \approx \sqrt{\frac{E\sigma tMa}{\rho yF}} = K_2 \cdot t^{1/2} \tag{15}$$

Eq. (15) is, apparently, identical with Eq. (5) for a classical Jansta and Dousek's model . Hence, the reaction kinetics at the C_xF_y | $M_{(Hg)}$ interface is rigorously described by Eq. (13), but (depending on the actual values of E_a and L) it may approach two limiting situations described by Eqs. (14) and (15), respectively . For solid fluoropolymers, the second limiting *scenario* (Eq. (15)) operates at all usual experimental conditions. The same holds for C_xF_y(g) | $Na_{(Hg)}$, where the growth rate is limited by the Na^+-conductivity of the carbonaceous film.

Table 2. Reaction of perfluorinated precursors with M amalgams (M = Li, Na, K). Rate constant, K_M (M= Li, Na, K) is quoted at 25°C unless stated otherwise. RS = reaction stoichiometry (the found consumption of M referred to that calculated for the total defluorination of the precursor); δ = doping level of carbon (calculated per carbon atom also for precursors containing nitrogen).

Precursor	K_{Li} [nm.s^{-1}]	Doping		Note/ (Ref. for K_{Li})
		RS [%]	δ	
C_6F_{14} Perfluorohexane	0.03	110	0.23	Ref.
C_4F_8 Perfluorocyclobutane	0.2	112	0.24	Ref.
C_6F_{12} Perfluorocyclohexane	0.002	109	0.18	Ref.
$C_{10}F_{18}$ Perfluorodecalin	0.5	111	0.20	Ref.
C_5F_8 Perfluorocyclopentene	7	113	0.21	Ref.
C_5F_8 Perfluorocyclopentene	2	-	-	0° C; Ref.
C_5F_8 Perfluorocyclopentene	0.3	-	-	-15° C; Ref.
C_6F_6 Perfluorobenzene	0.06	120	0.20	Ref.
$C_{10}F_8$ Perfluoronaphthalene	0.15	124	0.19	Ref.
$C_{10}F_8$ Perfluoronaphthalene	0.2	-	-	Ref.
$C_{12}F_{10}$ Perfluorobiphenyl	0.01	120	0.17	Ref.
C_6F_5CN Perfluorobenzonitrile	5	115	0.13	Ref.
C_5F_5N Perfluoropyridine	1	118	0.18	Ref.
$C_3F_3N_3$ Cyanuric fluoride	0.003	114	0.14	This work
C_4F_6 Perfluoro-2-butyne	(see text)	114	0.21	Ref.

Precursor	K_{Na} [nm.s$^{-1/2}$]	Doping		Note/ (Ref. for K_{Na})
		RS [%]	δ	
C_4F_8 Perfluorocyclobutane	2.9	106	0.12	Ref.
$C_{10}F_{18}$ Perfluorodecalin	5	119	0.34	Ref.
C_5F_8 Perfluorocyclopentene	9.5	111	0.18	Ref.
C_5F_8 Perfluorocyclopentene	9	-	-	Ref.
C_5F_8 Perfluorocyclopentene	18	-	-	40ºC;Ref.
$C_{10}F_8$ Perfluoronaphthalene	18[a]	120	0.16	Ref.
C_4F_6 Perfluoro-2-butyne	9	109	0.14	Ref.

Precursor	K_K [nm.s$^{-1/2}$]	Doping		
		RS [%]	δ	
C_5F_8 Perfluorocyclopentene	0.2	108	0.13	Ref.
$C_{10}F_8$ Perfluoronaphthalene	0.3	118	0.14	Ref.

[a] In early stages of reaction K_{Na}= 0.3 nm/s, see Ref. for details

Since the Li^+ conductivity is much higher, the reaction with $Li_{(Hg)}$ is controlled by the rate of the $C_xF_y(g)$ reduction at the film's surface. The fast transport of Li^+ does not obstruct the intrinsic rate of carbonization at the interface between the C_xF_y and the growing carbonaceous film . Consequently, the overall kinetics becomes controlled by the rate of interfacial carbonization, and the film grows linearly with time. This rule is violated only in the case of perfluoro-2-butyne, K_{Li} = 120 nm s$^{-1/2}$. The interpretation is straightforward: The carbonization of perfluoro-2-butyne is so fast, that the overall reaction is limited by the Li^+ transport in the growing film, as in the case of Na^+ transport. Apparently, the film thicknesses can be controlled with nanometer-precision simply by adjusting of the reaction time . The film is also ideally flat, as it grows on the surface of liquid amalgam .

2. ELECTROCHEMICAL PROPERTIES OF NANOCARBONS

Redox properties of nanocarbons, *viz*. carbon nanotubes, fullerenes and fullerene peapods, can be addressed either by investigation of chemical redox reactions with suitable electron acceptors/donors or by electrochemical methods. The latter strategy is easy, versatile and precise in terms of the defined conditions of charge-transfer . Fullerene peapods (C_{60}@SWCNT, C_{70}@SWCNT, etc.) were discovered in 1998 . Electrochemistry on peapods was studied in much less extent compared to the works on empty tubes and fullerenes. Nevertheless, there is a clear challenge to explore the electrochemical and chemical doping behavior of peapods. As both of the components of peapods, i.e. SWCNT and C_{60}/C_{70}, show specific redox response, these studies should address fundamental problems of electronic and redox properties of carbon nanostructures.

A common problem of nanocarbons consists in the fact that all the so far available SWCNT materials are complex mixtures of tubes of various chiralities, which are, moreover, bundled by intertube van der Waals bonds. The same holds for the derived materials, i.e. peapods and double walled carbon nanotubes (DWCNT) . Recently, we have developed a new simple method for deposition of isolated nanoribbons composed either of SWCNT,

DWCNT or fullerene (C_{60}) peapods on Au(111) surface . These nanoribbons are quite useful, as they exhibit characteristic Raman features of individual carbon nanostructures.

2.1. Optical and Raman spectroelectrochemistry on single walled carbon nanotubes

Since the pioneering work of Rao et al. , there has been great interest in charge-transfer doping of SWCNT. The electronic states of SWCNT contain van Hove singularities, which control many electronic and optical properties of SWCNT. We can distinguish four sets of singularities: filled valence-band semiconducting ($v_s^{1,2,3\cdots}$), empty conduction band semiconducting ($c_s^{1,2,3\cdots}$) and analogous sets for metallic tubes ($v_m^{1,2,3\cdots}$, $c_m^{1,2,3\cdots}$) . Allowed optical transitions between singularities give rise to characteristic absorption bands in the optical (Vis-NIR) spectra . The same optical transitions are also responsible for large resonance enhancement of Raman scattering in SWCNT .

The population of singularities can be controlled electrochemically by applying certain potential on SWCNT in contact with an electrolyte solution . SWNCT exhibit reversible bleaching of the optical transitions between Van Hove singularities, if the potential moves from the open-circuit in negative or positive directions . The bleaching of optical transitions also causes reversible quenching of resonance Raman scattering of both radial breathing (RBM) and tangential displacement modes (G-modes) of SWCNT .

The Raman and Vis-NIR spectroelectrochemistry of SWCNT was studied in aqueous and acetonitrile solutions. To increase the electrochemical window in aqueous media towards negative potentials, a mercury electrode was also used as a support of SWCNT . Eventually, the spectroelectrochemical methodology was transferred to ionic liquids, *viz*. 1-butyl-3-methylimidazolium tetrafluoroborate or 1-butyl-3-methyl-imidazolium hexafluorophosphate . These media allow the broadest window of electrochemical potentials to be applied (-2.4 to 1.7 V *vs.* Fc/Fc^+). They present very stable, solvent-free electrolytes, which even permit *in-situ* spectroelectrochemical studies by Vis-NIR and Raman spectroscopy to be carried out .

SWCNT, fabricated by catalytic laser-ablation of graphite, show relatively narrow distribution of tube diameters between *ca.* 1.1-1.4 nm . On the other hand, the HiPco tubes with diameters between *ca.* 0.7 to 2 nm are ideal for investigation of chirality-selective effects . Efficient doping of wider tubes can be simply interpreted in terms of the chirality-selective transition energies between the Van Hove singularities . Consequently, the singularities of wider tubes are depleted/filled before those of narrower tubes, when the p-/n-doping progresses . The somewhat unexpected good doping of the narrowest tubes was ascribed to smaller van der Waals forces, keeping the bundle together and/or to the fact that the dopant/carbon ratio is relatively higher for thin tubes . Hence, the tubes of intermediate diameters (between 1 to 1.2 nm) are less doping-sensitive. This effect is conveniently followed by Raman spectroscopy, and can be interpreted by variation of the resonance condition depending on the tube chirality .

A significant advantage of electrochemical doping over the chemical redox doping consists in the fact, that one can easily follow the chirality-selective effects with rich selection

of compensating counterions. In general, the cathodic doping (compensated by cations in the double layer) leads to more pronounced attenuation, compared to anodic doping (compensated by extra anions in the double layer) . The charge compensation with 1-butyl-3-methylimidazolium cations in ionic liquid is less efficient than the charge compensation of alkylammonium or Li^+ cations in acetonitrile media. The most pronounced doping takes place in the presence of Li^+ cations. The alkylammonium cations show only small dependence on the alkyl type (methyl, butyl, octyl), albeit methyl is closer to Li, while octyl is closer to the bulky cations of ionic liquids .

The G-mode is blue-shifted upon anodic charging at larger potentials, which reflects the stiffening of the graphene mode if holes are introduced into the π band . The shifts of G-mode, generated by n-doping are more complex. In contrast to p-doping which always causes a blue-shift of the G-mode , the n-doping carried out chemically or electrochemically may cause both blue- or red-shifts depending on the counter-ion used (Li^+, K^+, Rb^+), doping level and the excitation wavelength. The interpretation is far from being consistent at the moment .

2.2. Optical and Raman spectroelectrochemistry on fullerene peapods

Electrochemical charge-transfer on fullerene peapods (C_{60}@SWCNT and C_{70}@SWCNT) was studied in 0.2 M $LiClO_4$ + acetonitrile and in 1-butyl-3-methylimidazolium tetrafluoroborate (ionic liquid) . The capacitance of peapods (C) was similar to that of empty SWCNT, i.e. *ca.* 40 F/g . For an ideal double layer capacitor, the change in number of electrons transferred per one carbon atom, Δf equals:

$$\Delta f = \frac{M_C C \Delta U}{F} \qquad (16)$$

where M_C is atomic weight of carbon, ΔU is potential difference and F is Faraday constant. Equation (16) yields Δf = 0.005 e^-/C-atom for ΔU = 1 V and C = 40 F/g. A one electron reduction of C_{60} represents Δf = 0.017 e^-/C-atom (for C_{70}: Δf = 0.014 e^-/C-atom). Hence, the redox-process C_{60}/C_{60}^- or C_{70}/C_{70}^- would correspond to *ca.* 3 times more electrons per C-atom compared to double layer charging of the wall. Cyclic voltammetry of C_{60}@SWCNT and C_{70}@SWCNT evidences that the electroreduction of intra-tubular C_{60}/C_{70} is hampered. Even a stronger chemical reduction of C_{60}@SWCNT with K-vapor was sluggish, starting with a charge transfer to the nanotube wall . However, the reaction propagates, and K-atoms may even be accommodated inside the peapod . This effect is specific for gaseous potassium only; an alternative redox process employing K-amalgam does not lead to any penetration of K into the peapod . Obviously, the charge compensation "through-wall" operating in amalgam-driven reactions and in electrochemistry is not sufficient, due to a limited double-layer capacity (cf. Eq. 16).

Similarly to empty SWCNT , peapods showed three optical bands: ($\nu_s^1 \rightarrow c_s^1$), ($\nu_s^2 \rightarrow c_s^2$), and ($\nu_m^1 \rightarrow c_m^1$) at open-circuit potential. No distinct optical transitions of C_{60}/C_{70} were found . Anodic polarization shifts the Fermi level, and the singularities are depleted in the sequence: c_s^1, c_s^2, c_m^1. Analogously, cathodic polarization leads to

sequential filling of the singularities: v_s^1, v_s^2, v_m^1. In both cases, the optical bands reversibly disappear in the same sequence . In ionic liquid, the Vis-NIR spectra of peapods can be recorded up to 2.45 V vs. Fc/Fc^+, while a new optical band appears at *ca.* 1.1-1.3 eV . It reminds the doping-induced transitions for heavily p-doped SWCNT ($v_s^n \rightarrow v_s^1$, $v_s^n \rightarrow v_s^2$ $n \geq 3$). Similar to the charging of SWCNT in acetonitrile electrolyte solution the absorbance switching is reversible and fast: *ca.* 90% of the absorbance shift occurs in times <1 s . The optical switching is driven by fast double-layer charging (cf. Eq. 16).

Raman spectra of electrochemically charged C_{60}@SWCNT and C_{70}@SWCNT roughly exhibit the expected Raman peaks of intratubular C_{60} and C_{70}. Both the $A_g(1)$ and $A_g(2)$ modes of C_{60} have an interesting satellite line at higher frequency . The Raman spectrum of C_{70} peapods is considerably more complicated, because of the lower symmetry of the C_{70} molecule (53 Raman active vibrations for the D_{5h} symmetry: $12A_1' + 22E_2' + 19E_1$) . Also in the case of C_{70} peapods, we can detect splitting of some lines: at 260 cm^{-1}, 450 cm^{-1} and 699 cm^{-1}. Cathodic doping of C_{60}@SWCNT causes overall decrease of Raman intensities. However, at positive potentials, we see an interesting *enhancement of Raman intensities of intratubular* C_{60}. The "anodic enhancement" is apparent for all C_{60} related modes, except the satellite lines of $A_g(1)$ and $A_g(2)$ modes, respectively.

Surprisingly, the "anodic enhancement" of intratubular C_{60} does not reproduce in C_{70}@SWCNT. All the relevant Raman modes of C_{70}-peas show the "normal" symmetric potential-dependence (as the RBM/G-mode), although not all the peapod-bands are equally sensitive to charging . As in C_{60}@SWCNT , doping discloses some lines, which are normally hidden in peapods by the overlapping D- and G-lines . The non-symmetric anodic Raman enhancement in C_{60}@SWCNT can be interpreted as follows: The LUMO level of C_{60} (t_{1u}) is unusually close to the Fermi level of SWCNT . Extra electrochemical charge interacts primarily with the peapod wall, causing the depletion/filling of states close to the Fermi level. This leads to symmetric anodic/cathodic bleaching of the RBM/G-mode intensities and the frequency shifts of G-mode. Cathodic charging of C_{60}@SWCNT causes that the extra electrons efficiently quench the HOMO-LUMO transition, but anodic charging virtually does not influence the electronic structure of C_{60}. We may also relate this effect to the known reluctance of C_{60} towards anodic oxidation .

In C_{70}@SWCNT, the LUMO is located above the conduction band of SWCNT. This is the case also for wider tubes, in which the intratubular C_{70} can rearrange from lying to standing configuration . Such a steric compensation is inherently excluded for C_{60} because of its spherical symmetry. The “thick” C_{60} peapods have their LUMO-band very near the Fermi level, while it can even be partly filled, and the Raman resonance is quenched. Anodic charging of

thick C_{60} peapods will deplete the half-filled LUMO, which efficiently enhances the overall Raman intensity.

Further peculiar effects in C_{60} peapods were disclosed by a combination of chemical doping with K-vapor and by electrochemistry . The fullerene $A_g(2)$ mode softens to *ca.* 1428 cm^{-1} in the K-treated peapod, indicating intratubular C_{60}^{6-} . Surprisingly, the intratubular C_{60}^{6-} is not fully recoverable to neutral C_{60} even after anodic oxidation at 1.5 V vs. Ag/AgCl, when part of fullerene still survives in the C_{60}^{4-} state . This evidences that K^+ may also partly occupy the interior of peapod . Iijima et al recently confirmed this conclusion by direct TEM imaging of K inside peapods.

2.3. Optical and Raman spectroelectrochemistry on double-walled carbon nanotubes

Double-walled carbon nanotubes (DWCNT) can be conveniently prepared by from peapods by vacuum pyrolysis or by laser photolysis . Chemical doping of DWCNT by Br_2 was first studied by Eklund et al. . The DWCNT represent very attractive material for optical and Raman spectroelectrochemistry, as the doping-induced effects can be studied *selectively for outer tubes or inner tubes*, respectively . The outer tubes exhibit similar optical (Vis-NIR) spectral features as those observed for SWCNT, but the inner tubes manifest themselves by characteristic splitting of the band around 1.3 eV. Electrochemical charging causes reversible bleaching of optical transitions, while the behavior of outer tube resembles that of SWCNT. As expected, the inner tubes are less sensitive to electrochemical charging, since only small amount of doping charge is located at the inner tubes.

The RBM of outer/inner tubes is clearly distinguishable already in pristine DWCNT, but the corresponding analysis of G-mode requires subsequent mathematical deconvolution. The Raman spectroelectrochemistry in acetonitrile electrolyte solution and in ionic liquids allows interesting alternative, i.e. “electrochemical deconvolution” of the G-mode, especially at anodic potentials. The reason consists in larger doping-sensitivity of the outer tube, whose G-band is more blue-shifted than the G-band of the inner tube . Raman spectroelectrochemistry of DWCNT also points at very useful properties of the G’ mode, which splits into two components assigned to inner/outer tubes already in pristine DWCNT . This mode is highly dispersive, and doping-sensitive also in SWCNT. The charging-induced bleaching of G’ mode further confirms that the inner tubes are less sensitive compared to the outer tubes .

Also the doping-induced attenuation of the sharp peaks of RBM of inner tubes is relatively smaller than that of outer tubes. This behavior is phenomenologically equivalent to that of peapods, where we also trace sluggish response of the intratubular species to electrochemical perturbations (Section 2.2) . A more detailed analysis of doping of inner tubes reveals a similar diameter-sensitivity as that for SWCNT . This conclusion is surprising, as the arguments for complex and non-symmetric potential/intensity profiles in SWCNT bundles , i.e. the counterion insertion and solvation , are inherently nontransferable to the inner tubes of DWCNT. These questions must be, therefore, addressed in terms of chirality-dependent matching of resonance condition, which may or may not be diameter-selective as in SWCNT (cf. Section 2.1) .

References to Part B. (References 1-15 are attached to the thesis *in extenso*)